The Evolution of Radio Galaxies at Intermediate Redshift

M. J. I. Brown

National Optical Astronomy Observatory, P.O. Box 26732, 950 North Cherry Avenue, Tucson, AZ 85726, USA

mbrown@noao.edu

R. L. Webster

School of Physics, University of Melbourne, Parkville, Victoria 3010, Australia

and

B. J. Boyle

Anglo-Australian Observatory, P.O. Box 296, Epping, NSW 1710, Australia

ABSTRACT

We describe a new estimate of the radio galaxy 1.4GHz luminosity function and its evolution at intermediate redshifts ($z \sim 0.4$). Photometric redshifts and color selection have been used to select $B_J < 23.5$ early-type galaxies from the Panoramic Deep Fields, a multicolor survey of two $25\square^{\circ}$ fields. Approximately 230 radio galaxies have then been selected by matching early-type galaxies with NVSS radio sources brighter than 5mJy. Estimates of the 1.4GHz luminosity function of radio galaxies measure significant evolution over the observed redshift range. For an $\Omega_M = 1$ cosmology the evolution of the radio power is consistent with luminosity evolution where $P(z) \sim P(0)(1+z)^{k_L}$ and $3 < k_L < 5$. The observed evolution is similar to that observed for UVX and X-ray selected AGN and is consistent with the same physical process being responsible for the optical and radio luminosity evolution of AGN.

Subject headings: galaxies: active — galaxies: evolution — galaxies: luminosity function — radio continuum

1. Introduction

Evolution of radio sources is required to explain the observed number of radio sources and the redshift distribution of radio sources with observed optical counterparts (Longair 1966; Condon

1984; Peacock 1985). Radio emission from high redshift AGN is detectable in wide-field radio sky surveys and the optical counterparts of some $z > 3$ radio-loud QSOs can be detected on Schmidt photographic plates. However, most radio-loud AGN are radio galaxies and at $z \sim 0.5$ their faint optical counterparts ($B_J \sim 23$) make it difficult to obtain the large spectroscopic samples required to measure the evolution of the luminosity function.

Several previous samples of radio galaxies with redshifts are summarized in Table 1. To date, most estimates of the radio galaxy luminosity function have relied on catalogues limited to bright radio flux limits (Kuehr et al. 1981; Wall and Peacock 1985; Dunlop et al. 1989) or bright optical flux limits (Condon 1989; Sadler et al. 1989; Machalski and Condon 1999). These catalogues contain relatively few radio galaxies (as opposed to radio-loud QSOs) at $z > 0.2$, and consequently shed little light on the radio galaxy luminosity function and its evolution at these redshifts. Samples that have attempted to extend our knowledge of the radio galaxy luminosity function at $z \gtrsim 0.2$, by extending the identification of mJy radio sources to faint optical magnitudes ($B > 22$) have been limited to relatively small samples of objects (10-60 galaxies) due to the difficultly of obtaining follow-up spectroscopy. As a result, estimates of the radio galaxy luminosity function and evolution obtained from these samples are still subject to significant uncertainty.

With photometric redshifts and color selection, it is possible select and estimate the redshifts of faint early-type galaxies in multicolor imaging surveys (Brown et al. 2000). By matching early-type galaxies with sources from the radio catalogues, it is possible to compile a large uniformly selected catalogue of radio galaxies to measure the evolution of the radio galaxy luminosity function. As the radio galaxies are selected from deep wide-field imaging data, a large catalogue of radio-quiet galaxies is also available to measure the environments of the radio galaxies (Brown et al. 2001).

2. The Panoramic Deep Fields

The Panoramic Deep Fields (Brown 2000) are $5° \times 5°$ images of the South Galactic Pole (SGP) and UK Schmidt field 855 (F855). The images were produced by stacking SuperCOSMOS scans of UK Schmidt photographic plates in U, B_J, R and I bands. Object detection, instrumental photometry and faint object star-galaxy classifications were determined with SExtractor (Bertin and Arnouts 1996). Photometric calibration of the data was determined with CCD images and published photometry with corrections for dust extinction being derived from the dust maps of Schlegel et al. (1998). The final galaxy catalogues are complete to $B_J \sim 23.5$ and $R \sim 22$. Brown (2000) provides a detailed description of the data reduction and calibration of the Panoramic Deep Fields.

Photometric redshifts were calibrated using the polynomial fitting method of Connolly et al. (1995) and ~ 700 Panoramic Deep Field galaxies with spectroscopic redshifts available from the NED database (Brown et al. 2000). Comparison of the photometric redshifts of radio galaxies with spectroscopic redshifts showed that radio galaxy redshifts were systematically underestimated by

$\sim 15\%$. This is almost certainly due to radio galaxies being more luminous and having slightly bluer colors than other early-type galaxies (Sadler et al. 1989; Govoni et al. 2000) To correct for this, the photometric redshifts of radio galaxies in this paper were increased by 15% and Figure 2 shows there is good agreement between the corrected photometric and spectroscopic redshifts.

3. Selection of Radio Galaxies

The radio galaxy sample consists of Panoramic Deep Field galaxies which are associated with objects in the NVSS source catalogue (Condon et al. 1998). $B_J - R$ color and photometric redshifts were used to select $B_J < 23.5$ galaxies which are redder than a non-evolving Sbc where the Sbc colors were determined with the $k-$corrections of Coleman et al. (1980). The optical galaxies were then matched to radio sources from the NVSS source catalog. The selection of early-type galaxies removes contamination of the radio galaxy sample by QSOs and starbursts. If unified models of radio-loud AGN (Barthel 1989) are valid, the removal of QSOs from the sample removed radio galaxies viewed at certain orientations. However, as the galaxy photometric redshifts are not usable for QSOs, the removal of QSOs from the sample allowed the measurement of radio galaxy evolution without spectroscopic redshifts.

As the evolution of the radio galaxy population was studied, the criterion used for matching radio and optical sources could not be a function of redshift. High completeness was also required to prevent the estimate of the luminosity function being dominated by corrections for incompleteness. Low contamination of the sample was required so estimates of the luminosity function and radio galaxy environments would not be dominated by galaxies not associated with radio sources.

The brightest NVSS source catalogue positions have 1σ error estimates of $\sim 1''$ while the faintest (~ 2.5mJy) source positions have errors of $\gtrsim 10''$ (Condon et al. 1998). The sky surface density of $B_J < 23.5$ galaxies which meet the color selection selection criterion is $\sim 0.5/\square'$ so $\gtrsim 40\%$ of ~ 2.5mJy sources have an unassociated optical galaxy within 3σ of the radio source position. To prevent the catalogue being dominated by spurious matches to faint radio sources, the radio flux limit was set to 5mJy which is slightly brighter than completeness limit of the NVSS catalogue.

The Panoramic Deep Fields contain $\sim 9 \times 10^4$ early-type galaxies and $\sim 10^4$ radio sources making the manual selection of radio galaxies prohibitively time consuming. An obvious automated criterion for selecting optical counterparts to radio sources is to match objects within $\sim 3\sigma$ of the radio source centroid. However, as many extragalactic radio sources have extended emission, this will be incomplete for a significant fraction of radio sources. Selection criterion using only the angular separation between radio and optical sources can select a large fraction of all radio sources. However, for a fixed angular scale, the projected distance increases with redshift introducing selection effects which are a function of redshift. Large radio sources will be excluded at low redshift but will be included at high redshift where the angular size of the radio sources is less than the selection criterion.

As the optical counterparts of radio sources are physical associations, a selection criterion based on the physical separation of the optical and radio sources can be used to select radio galaxies. While the NVSS catalogue does not contain redshift information, photometric redshifts can be used to estimate the redshifts of optical galaxies and the projected distance between the optical and radio sources. As the size (in physical coordinates) of radio sources does not rapidly evolve between $z \sim 1$ and $z \sim 0$ (Buchalter et al. 1998), a selection criterion using a fixed projected distance should not introduce selection effects which are a function of redshift.

To determine the projected distance used as the selection criterion for optical counterparts, the distribution of projected distances between NVSS sources and optical galaxies within $30''$ of NVSS sources was measured and is plotted in Figure 1. The number of optical counterparts declines rapidly on scales $< 20h^{-1}\mathrm{kpc}$ ($h \times 100\mathrm{kms}^{-1}\mathrm{Mpc}^{-1} \equiv H_0$) after which the distribution has a long tail. Approximately 25% of the NVSS sources with early-type galaxies within $30''$ have more than one early-type counterpart which is consistent with much of the tail in Figure 1 being contamination. To reduce the contamination, optical galaxies $> 20h^{-1}\mathrm{kpc}$ from NVSS sources were excluded from the radio galaxy sample. A complete list of the radio galaxy sample is provided in Table 2.

The completeness of the selection criterion was estimated by applying the $20h^{-1}\mathrm{kpc}$ criterion to radio galaxies from the Las Campanas Redshift Survey identified by Machalski and Condon (1999). Approximately 85% of radio galaxies identified by Machalski and Condon (1999) were selected with the $20h^{-1}\mathrm{kpc}$ criterion. Fluxes in the NVSS source catalogue are estimated by fitting elliptical Gaussians to the radio emission and for $\sim 5\%$ of radio galaxies where the fits are poor, the fluxes disagree with Machalski and Condon (1999) by $> 5\%$. At $z < 0.05$, an increasing fraction of radio galaxies have radio emission resolved into multiple components by the NVSS resulting in $\sim 50\%$ of radio galaxies having source catalogue flux estimates which disagree with Machalski and Condon (1999).

While contamination is low with the $20h^{-1}\mathrm{kpc}$ selection criterion, it is still present in the radio galaxy catalogue. To prevent these objects from biasing the estimate of the luminosity function, a control sample was constructed by randomly repositioning the radio sources and matching them to the galaxy catalogue. This process was repeated 10 times so the control sample size was large enough to not be a significant source of noise in the estimate of the luminosity function.

Approximately 2% of radio sources with optical counterparts have 2 optical counterparts resulting in ambiguous redshift estimates. As this is a small fraction of the total catalogue, rejecting these objects from the radio galaxy and control samples only reduced the completeness of the sample by 4% and did not significantly bias estimates of the evolution of radio galaxies. The estimates of the space density and luminosity function parameters were renormalized to account for the 2% of radio galaxies removed from the catalogue. The final catalogue of radio galaxies contains 230 objects while the control sample (generated with 10 times as many radio sources) contains 229 objects.

4.   Redshift Distribution

The B_J and R Hubble diagrams for the optical counterparts of NVSS sources are shown in Figure 3. There is a strong correlation between redshift and magnitude though this is partially due to the use of photometric redshifts which result in objects with the same multicolor photometry having the same redshift estimate. The R band Hubble diagram shows evidence of incompleteness at $z > 0.55$ due to the B_J magnitude limit. As the apparent magnitude of a $M_{B_J} \sim -20$ elliptical at $z \sim 0.55$ is $B_J \sim 23$, this is not unexpected. As the incompleteness at $z > 0.55$ could significantly bias estimates of radio galaxy evolution, the sample was limited to redshifts $z < 0.55$. At low redshifts, the errors of the photometric redshifts are comparable to the redshift estimates resulting in large errors for the estimates of the radio power. To prevent these objects from introducing errors into the estimate of the luminosity function, only the 196 radio galaxies with $0.10 < z < 0.55$ were used to estimate the luminosity function. The redshift distributions of the radio galaxy sample, the Parkes selected regions(Dunlop et al. 1989) and Phoenix(Hopkins et al. 1998) are shown in Figure 4. The size of the Panoramic Deep Fields results in an improved estimate of the radio galaxy luminosity function at $z \sim 0.4$ and the broad redshift distribution has allowed the evolution of $z < 0.55$ radio galaxies to be measured.

5.   Color Distribution

The color selection criterion applied to the radio galaxy candidates will affect the sample completeness at some level. If a large fraction of radio galaxies have colors bluer than the selection criterion, significant uncertainty is introduced into estimates of the luminosity function and its evolution. The colors of galaxies in the radio galaxy sample are shown as a function of redshift in Figure 5. While most radio galaxies have red colors, some do have colors similar to the selection criterion. However, this could be due to contamination which is comprised mostly of blue galaxies which dominate the faint galaxy population.

The estimated restframe colors of the radio galaxy sample are plotted in Figure 6. Restframe colors were estimated with linear extrapolations from the E and Sbc $k-$corrections from Coleman et al. (1980). The peak of the distribution is ~ 0.2 magnitudes redder than the $B_J - R = 1.01$ selection criterion. For comparison, the distribution of radio galaxy colors from Govoni et al. (2000) is also shown. If Govoni et al. (2000) sample is representative of all radio galaxies, then $\sim 85\%$ of radio galaxies were selected by the color selection criterion. However, the distributions in Figure 6 are not identical and a systematic $\delta(B_J - R) = 0.1$ difference between the Govoni et al. (2000) and Panoramic Deep Field colors could alter the completeness by $\sim 10\%$. For the remainder of the paper, the incompleteness due to the color selection criterion is assumed to be 15%.

6. The 1.4 GHz Luminosity Function

The restframe radio power of the sources was estimated with

$$\log P_{1.4}(\mathrm{WHz}^{-1}) = \log S_{1.4}(\mathrm{mJy}) - (1 - \alpha_r)\log(1 + z) + 2\log D_l(\mathrm{Mpc}) + 17.185 \qquad (1)$$

where $S_{1.4}$ is the observed 1.4GHz radio flux, D_l is the luminosity distance and α_r is the radio spectral index which is assumed to be 0.7. The radio luminosity function was estimated with

$$\Phi(P_{1.4}) = \sum_i \frac{1}{V_{max,i}} \qquad (2)$$

(Schmidt 1968) where $V_{max,i}$ is the maximum comoving volume in which the ith source would be included in the sample. The value of $V_{max,i}$ is given by

$$V_{max,i} = \Omega \eta_i \frac{c}{H_0} \int_{z_{min}}^{z_{max}} \frac{dV_c}{dz} dz \qquad (3)$$

where Ω is the survey area, η_i is the completeness of the survey for sources with the properties of source i, z_{min} and z_{max} are the minimum and maximum redshifts where source i would be included in the sample and V_c is the comoving volume. The values of z_{min} and z_{max} were set by the bright and faint flux limits (optical and radio) for the sample and the lower and upper limits for the redshifts over which the luminosity function is determined.

The radio luminosity function of radio galaxies for $0.10 < z < 0.30$ and $0.30 < z < 0.55$ is shown in Figure 7 and listed in Table 3. To be consistent with previous work, the estimates of the luminosity function have been determined with $\Omega_M = 1$ and $H_0 = 100\mathrm{kms}^{-1}\mathrm{Mpc}^{-1}$. The $0.10 < z < 0.30$ space density is comparable to the low redshift samples of Sadler et al. (1989) and Machalski and Godlowski (2000) at $P_{1.4} > 10^{23}\mathrm{WHz}^{-1}$. Machalski and Godlowski (2000) may suffer incompleteness at $P_{1.4} < 10^{23}\mathrm{WHz}^{-1}$ as their estimate of the space density decreases with decreasing radio power. The space density of $0.30 < z < 0.55$ radio galaxies is significantly higher than the low redshift samples which is consistent with evolution occurring over the observed redshift range.

To measure the evolution of the radio galaxy luminosity function, the data was been fitted with a 2 power-law function

$$\Phi(P)d(\log P) = C^* \left[\left(\frac{P^*(z)}{P} \right)^{\alpha} + \left(\frac{P^*(z)}{P} \right)^{\beta} \right]^{-1} d(\log P) \qquad (4)$$

(Boyle et al. 1988; Dunlop and Peacock 1990). The evolution of the luminosity function was assumed to be pure luminosity evolution where

$$P^*(z) = P^*(0)(1 + z)^{k_L} \qquad (5)$$

(Boyle et al. 1988). The best-fit values for the C^*, $P^*(0)$, α, β and k_L were obtained by minimizing

$$S = -2\ln L \tag{6}$$

(Marshall et al. 1983) where L is the likelihood. The value of S is given by

$$S = -2\sum_{i=1}^{N_{rg}} \ln[\Phi(P, z_i)] + 2f\sum_{i=1}^{N_c} \ln[\Phi(P, z_i)] + 2\int\int \Phi(P, z)\Omega(P, z)\frac{dV}{dz}dzdP \tag{7}$$

where N_{rg} is the number of radio galaxies in the sample, N_c is the number of control objects and f is the number of radio sources used to produce the radio galaxy catalogue divided by the number of radio sources used to generate the control catalogue. Error estimates for the measured parameters were determined by computing ΔS for each parameter in turn while allowing the other values for the parameters to float (Lampton et al. 1976; Boyle et al. 1988). The errors quoted for the remainder of the paper were determined for $\Delta S = 1$ which is equivalent to 1σ. The goodness-of-fit of the model was tested using the 2D Kolmogorov-Smirnoff (KS) statistic described by Peacock (1983).

The best-fit estimate of the luminosity function is shown in Figure 8 and the estimates of luminosity function parameters and the KS probability are listed in Table 4. To allow comparison with low redshift samples, the radio power of sources used to estimate the space density have been divided by the estimate of the luminosity evolution. The luminosity function model is comparable to estimates of the luminosity function at low redshift. Also, as shown in Figure 4, the model is a good approximation to the observed redshift distribution of Panoramic Deep Field radio galaxies.

The estimates of the luminosity function parameters are affected by Malmquist bias due to errors in the radio flux and redshift estimates. To correct for this, artificial datasets of radio galaxies were generated using 2 power-law functions. The fluxes and redshifts were then scattered assuming their error distributions can be approximated by Gaussians. The distribution of 1σ values for the radio flux error distribution were determined using the error estimates provided by the NVSS source catalogue. For the photometric redshifts, the errors were estimated by computing the rms of the difference between photometric and spectroscopic redshifts as a function of redshift for early-type galaxies. The parameters which reproduced the observed luminosity function are listed in Table 4. With the exception of β, most parameters changed by $\lesssim 1\sigma$ and as shown in Figure 8, the estimate of the luminosity function at $z \sim 0$ is comparable the original estimate.

The estimate of the luminosity function and its evolution assumes that the radio galaxy catalogue is dominated by steep spectrum radio sources which is consistent with previous estimates of the luminosity function (Dunlop and Peacock 1990). However, if a significant fraction of the radio galaxy catalogue are flat-spectrum sources, a smaller value of α_r would be more appropriate for estimating the radio powers and the luminosities of the $z \sim 0.5$ radio galaxies would be significantly decreased. However, as shown in Table 4, decreasing the value of α_r to 0.5 only decreases the estimate of k_L by $\sim 1\sigma$.

The estimates of the luminosity evolution are comparable to previous estimates of the evolution of radio-loud AGN including QSOs (Dunlop and Peacock 1990). The similarity of radio-loud QSO and radio galaxy evolution is consistent with the unified theory of radio-loud AGN (Barthel 1989) where radio-loud QSOs and radio galaxies are the same class of object observed at different orientations. The radio evolution of radio galaxies is also similar to the evolution of radio-quiet AGN in the optical and X-ray (Boyle et al. 1988, 1994), starburst galaxies in the radio (Rowan-Robinson et al. 1993) and the star formation rate in the UV (Lilly et al. 1996).

While the similarity of the luminosity function and its evolution to previous work is not unexpected, it does confirm the ability of the techniques used in this work to estimate the radio galaxy luminosity function. If the color selection and photometric redshifts are used to select radio galaxies from deep 4-m imaging, it will be possible to accurately measure the decline of the $z > 4$ radio-loud AGN luminosity function with redshift and place constraints on the epoch of formation of AGN. The same techniques will also allow wide-field surveys to improve estimates of the $z \sim 0.2$ radio galaxy luminosity function, clustering and environments.

7. Summary

The Panoramic Deep Fields and the NVSS have been used to compile a catalogue of $B_J < 23.5$ radio galaxies. In this paper we report a new estimate of the radio galaxy luminosity function at $z > 0.1$ based on this sample. Radio fluxes, multicolor photometry and photometric redshifts have been used to select 230 radio galaxies over $50\square^\circ$. By matching radio sources to optical counterparts with selection criterion that are a function of projected distance, radio galaxies are selected with high completeness without introducing a strong bias as a function of redshift. There is significant evolution of the radio galaxy luminosity function at $z < 0.55$ which can be parameterized by luminosity evolution where $P(z) \sim P(0)(1+z)^{k_L}$ where $3 < k_L < 5$. The observed evolution of radio galaxies is consistent with the same physical process being responsible for the evolution of radio galaxies and radio-quiet AGN. As the estimate of the luminosity function does not require large numbers of spectroscopic redshifts, it will be possible to apply the same techniques to multicolor surveys where the time required to obtain large numbers spectroscopic redshifts is prohibitive.

8. Acknowledgments

REFERENCES

Barthel, P.D., 1989, ApJ, 336, 606

Bertin E., and Arnouts S. 1996, A&AS, 117, 393

Boyle, B.J., Shanks, T., and Peterson, B.A., 1988, MNRAS, 238, 957

Boyle, B.J., Shanks, T., Georgantopoulos, I., Stewart, G.C., and Griffiths, R.E., 1994, MNRAS, 271, 639

Brown, M.J.I. 2000, PhD Thesis, University of Melbourne

Brown, M.J.I., Boyle, B.J., and Webster, R.L. 2000, AJ, submitted

Brown, M.J.I., Boyle, B.J., and Webster, R.L. 2001, AJ, in preperation

Buchalter, A., Helfand, D.J., Becker, R.H., and White, R.L. 1998,

Coleman, G.D., Wu, C.C., and Weedman, D.W. 1980, ApJS, 43, 393 ApJ, 494, 503

Condon, J.J. 1984, ApJ, 287, 461

Condon, J.J. 1989, ApJ, 338, 13

Condon, J.J., Cotton, W.D., Greisen, E.W., Yin, Q.F., Perley, R.A., Taylor, G.B., and Broderick, J.J., 1998, AJ, 115, 1693

Connolly, A.J., Csabai, I., Szalay, A.S., Koo, D.C., Kron, R.G., and Munn, J.A., 1995, AJ, 110, 2655

Dunlop J.S., Peacock J.A., Savage A., Lilly S.J., Heasley J.N., and Simon A.J.B., 1989, MNRAS, 238, 1171

Dunlop, J.S., and Peacock, J.A. 1990, MNRAS, 247, 19

Govoni, F., Falomo, R., Fasano, G., and Scarpa, R. 2000, A&A, 353, 507

Hopkins A.M., Mobasher, B. Cram, L., and Rowan-Robinson, M., 1998, MNRAS, 296, 839

Kuehr H., Witzel A., Pauliny-Toth I.I.K., and Nauber U., 1981, A&As, 45, 367

Lampton, M., Margon, B., and Bowyer, S., 1976, ApJ, 208, 177

Lilly, S.J., Le Fevre, O., Hammer, F., and Crampton, D., 1996, ApJ, 460, L1

Longair, M.S. 1966, MNRAS, 133, 421

Machalski, J., and Condon, J.J., 1999, ApJS, 123, 41

Machalski, J., and Godlowski, W., 2000, A&A, 360, 463

Marshall, H.L., Avni, Y., Tananbaum, H., and Zamorani, G., 1983 ApJ, 269, 35

Matthews, T.A., Morgan, W.W., and Schmidt, M. 1964, ApJ, 140, 35

Mobasher, B., Cram, L., Georgakakis, A., and Hopkins, A. 1999, MNRAS, 308, 45

Peacock, J.A., and Wall, J.V., 1981, MNRAS, 194, 331

Peacock, J.A., 1983, MNRAS, 202, 615

Peacock, J.A., 1985, MNRAS, 217, 601

Rowan-Robinson, M., Benn, C.R., Lawrence, A., McMahon, R.G., and Broadhurst, T.J. 1993, MNRAS, 263, 123

Sadler, E.M., Jenkins, C.R., and Kotanyi, C.G. 1989, MNRAS, 240, 591

Sadler, E. M., McIntyre, V. J., Jackson, C. A., and Cannon, R. D., 1999, PASA, 16, 247

Schlegel, D.J., Finkbeiner D.P., and Davis M. 1998, ApJ, 500, 525

Schmidt, M. 1968, ApJ, 151, 393

Wall J.V., and Peacock J.A., 1985, MNRAS, 216, 173
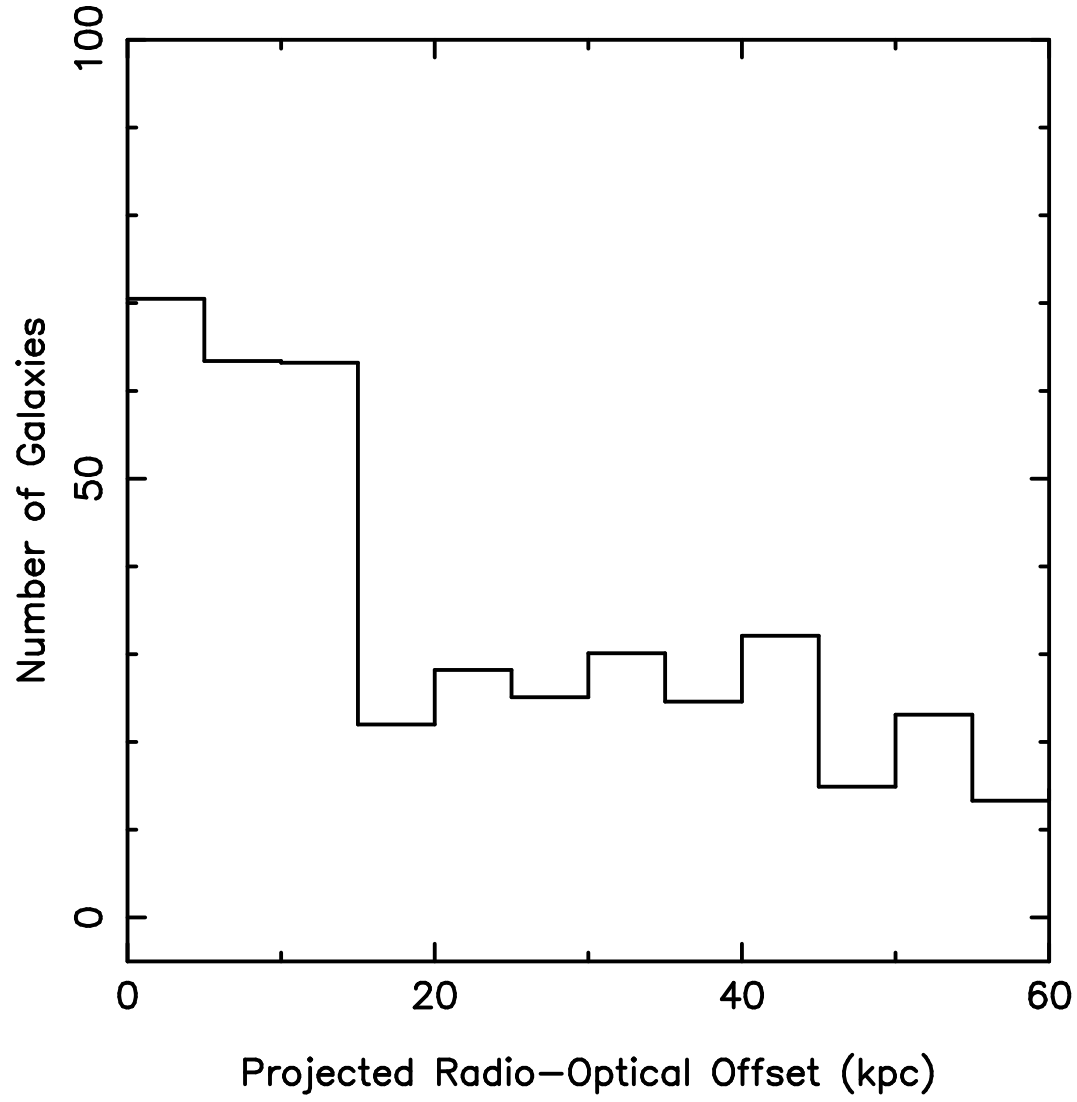
Fig. 1.— The projected distances between radio sources and optical galaxies with angular separations $< 30''$.
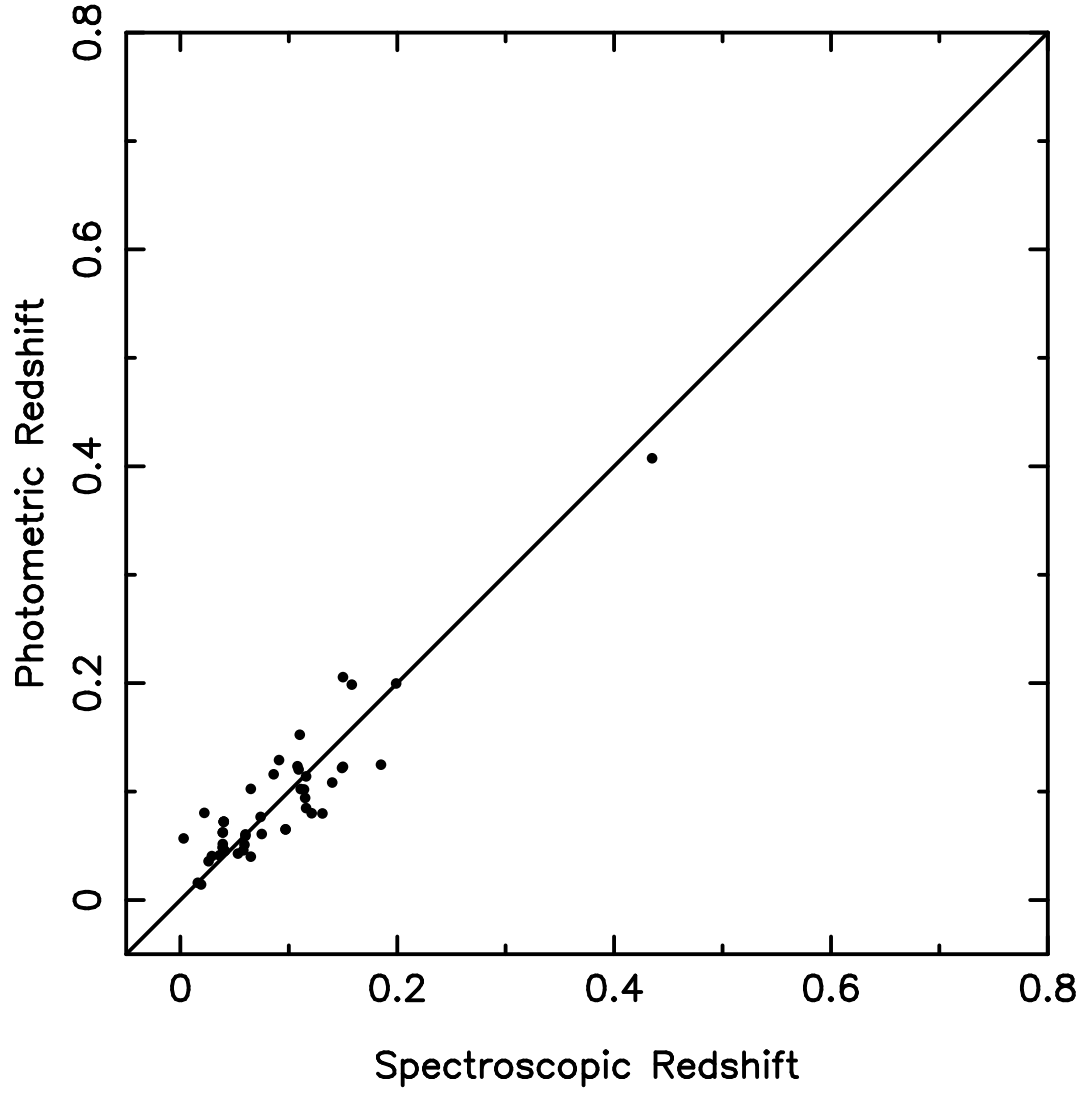
Fig. 2.— A comparison of photometric and spectroscopic redshifts of red galaxies which have been matched to the NVSS catalogue. The photometric redshifts for radio galaxies are 15% larger than the redshifts of radio-quiet galaxies with the same multicolor photometry. A detailed discussion of the calibration of the photometric redshifts is provided by Brown et al. (2000).
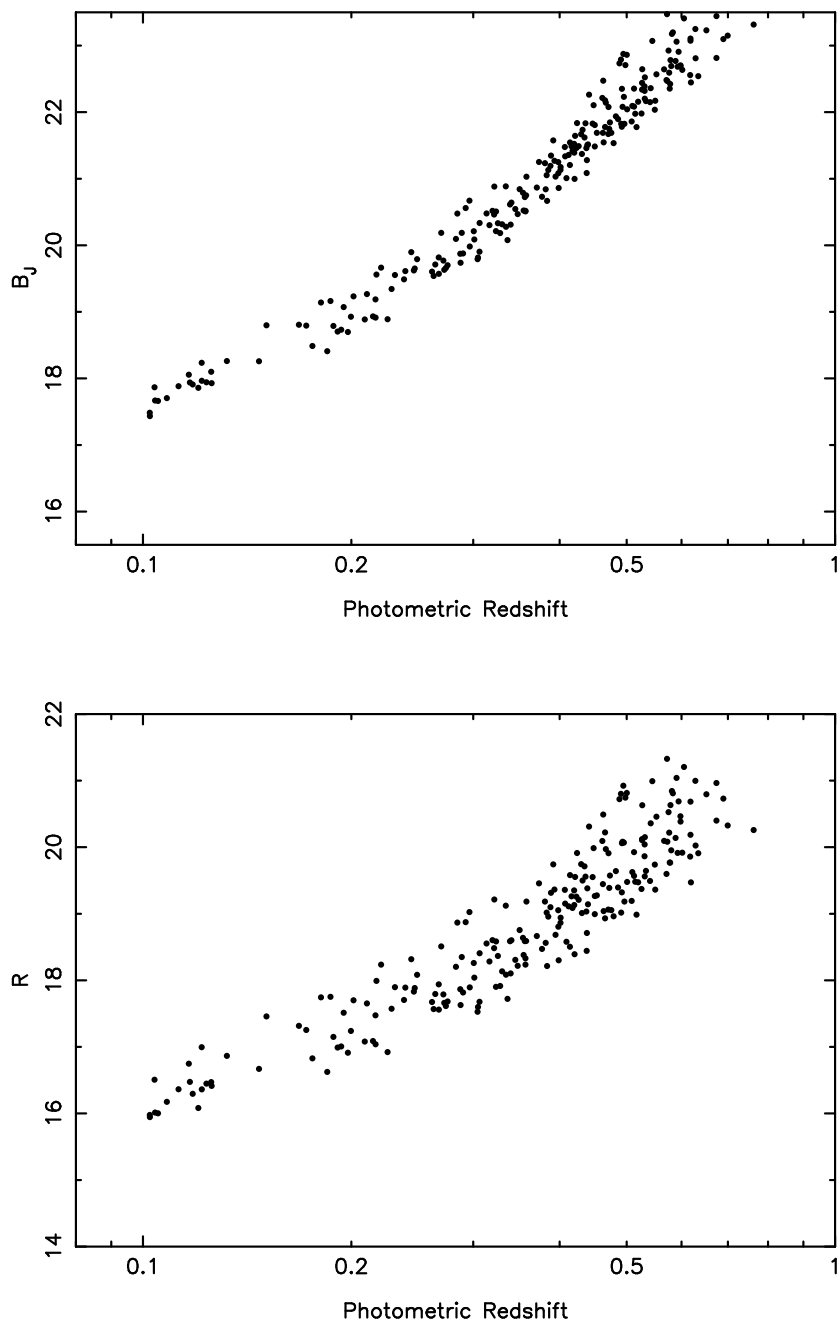
Fig. 3.— The B_J and R Hubble diagrams of $B_J < 23.5$ radio-galaxies in the Panoramic Deep Fields.
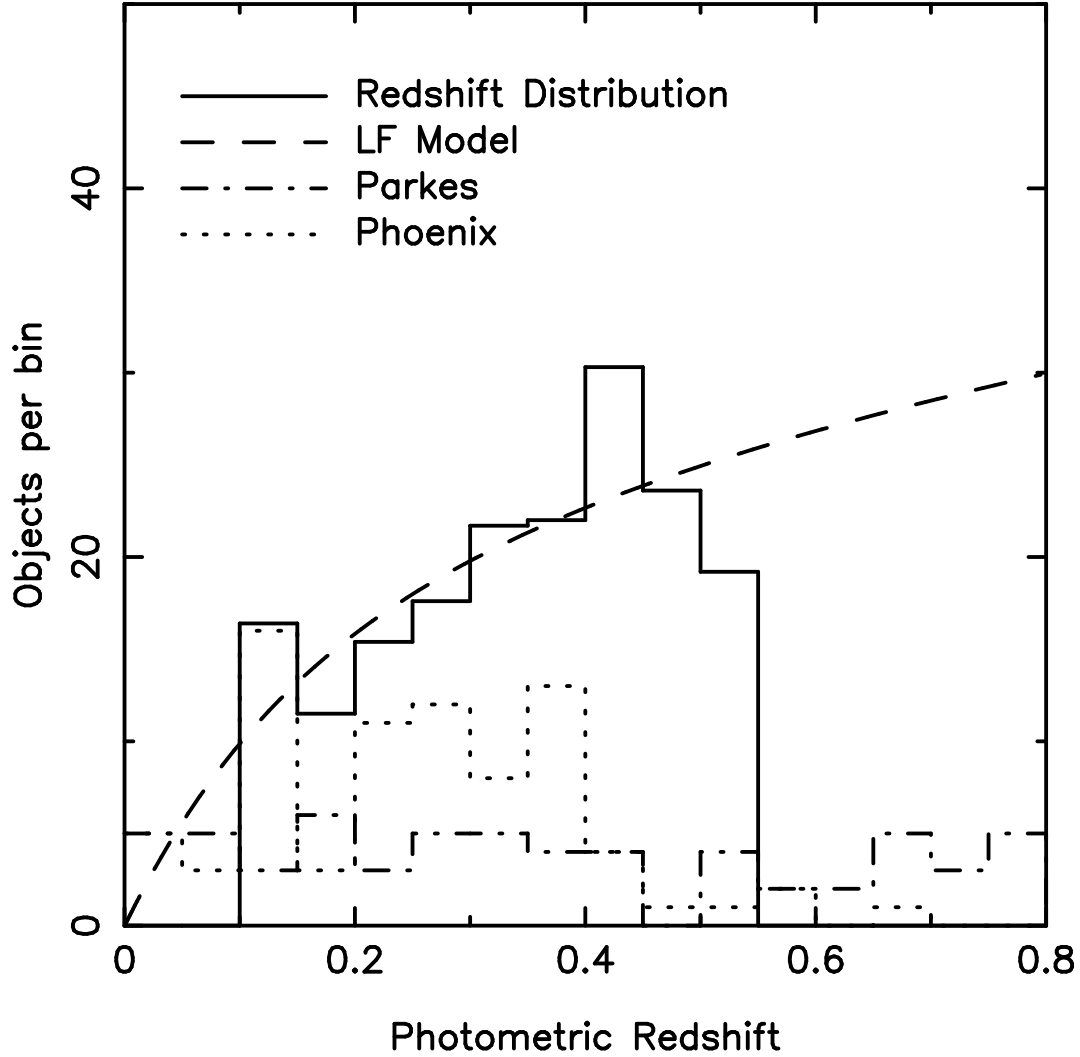
Fig. 4.— The radio galaxy redshift distributions of the Panoramic Deep Fields, Parkes selected regions(Dunlop et al. 1989) and Phoenix(Hopkins et al. 1998). The large size of the Panoramic Deep Fields allows it to accurately measure the radio galaxy luminosity function at intermediate redshifts. A model for the Panoramic Deep Fields redshift distribution determined with the luminosity function parameters in Table 4 is shown with the dashed line.
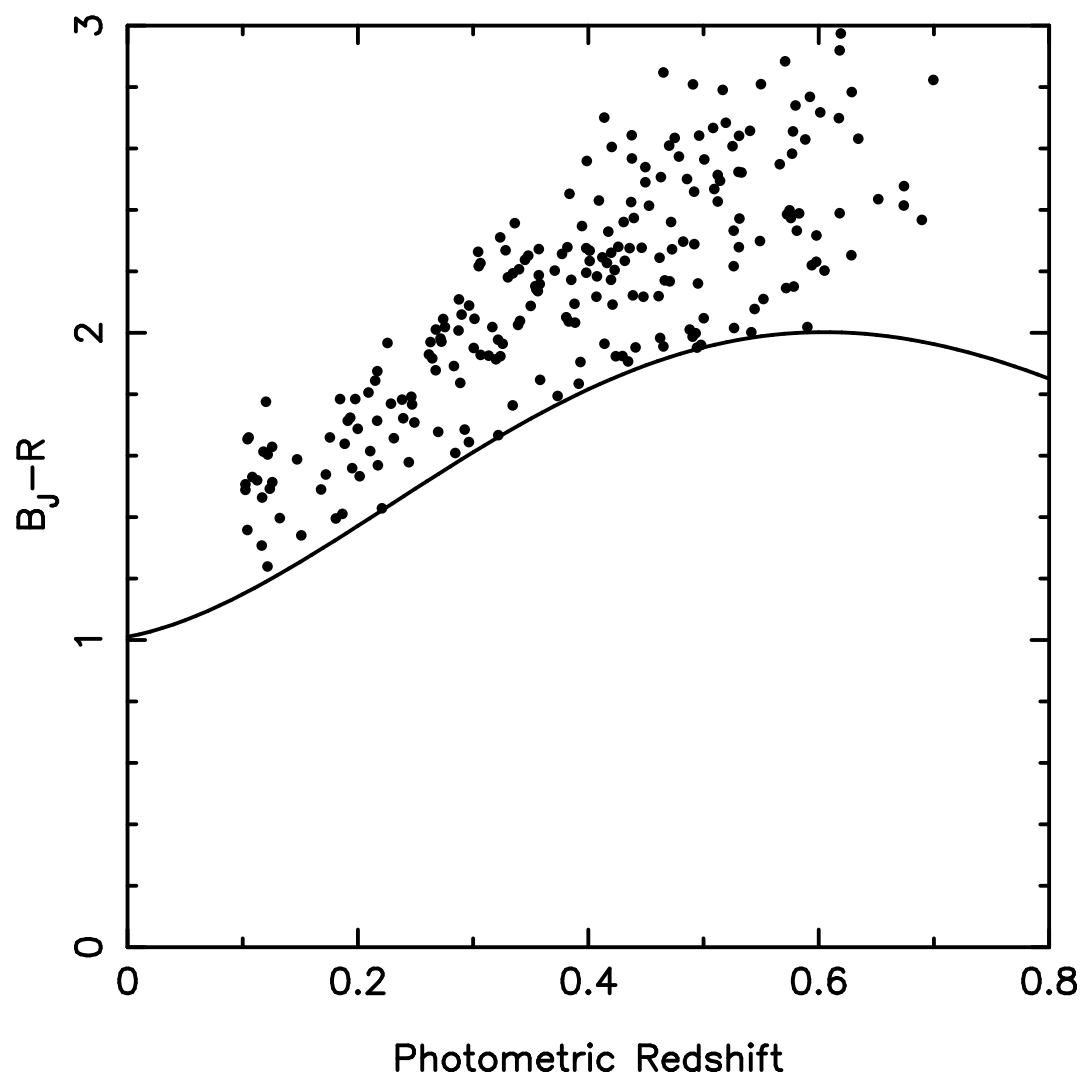
Fig. 5.— The colors of radio galaxies as a function of photometric redshift. The Sbc color selection criterion is shown with the curved line. Most radio galaxies have $B_J - R$ colors significantly redder than the selection criterion.
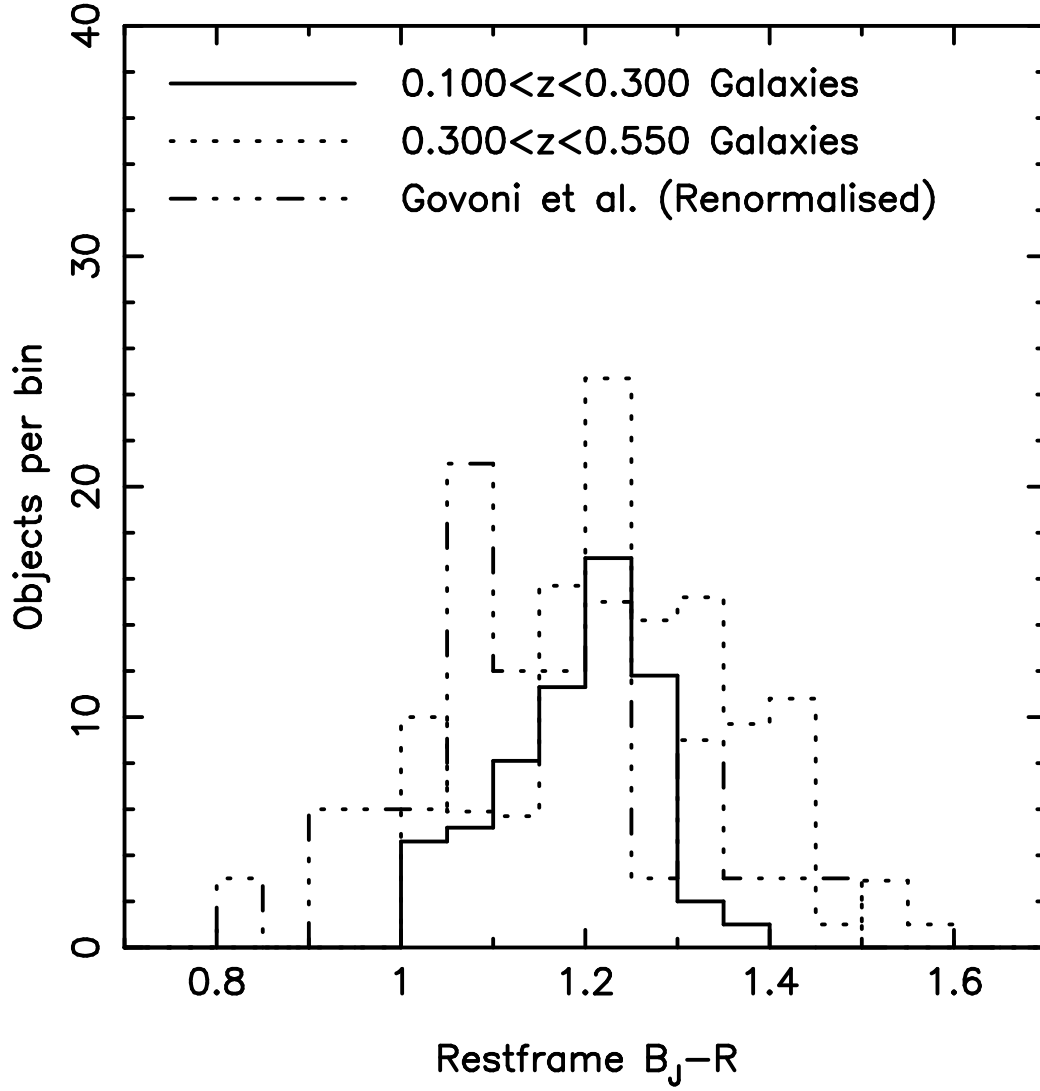
Fig. 6.— The restframe $B_J - R$ colors of the radio galaxy sample and Govoni et al. (2000). The control sample has been subtracted from the radio galaxy sample distribution to remove the affects of contamination. The number of objects in the Govoni et al. (2000) has been multiplied by 3 to aid comparison of the samples.
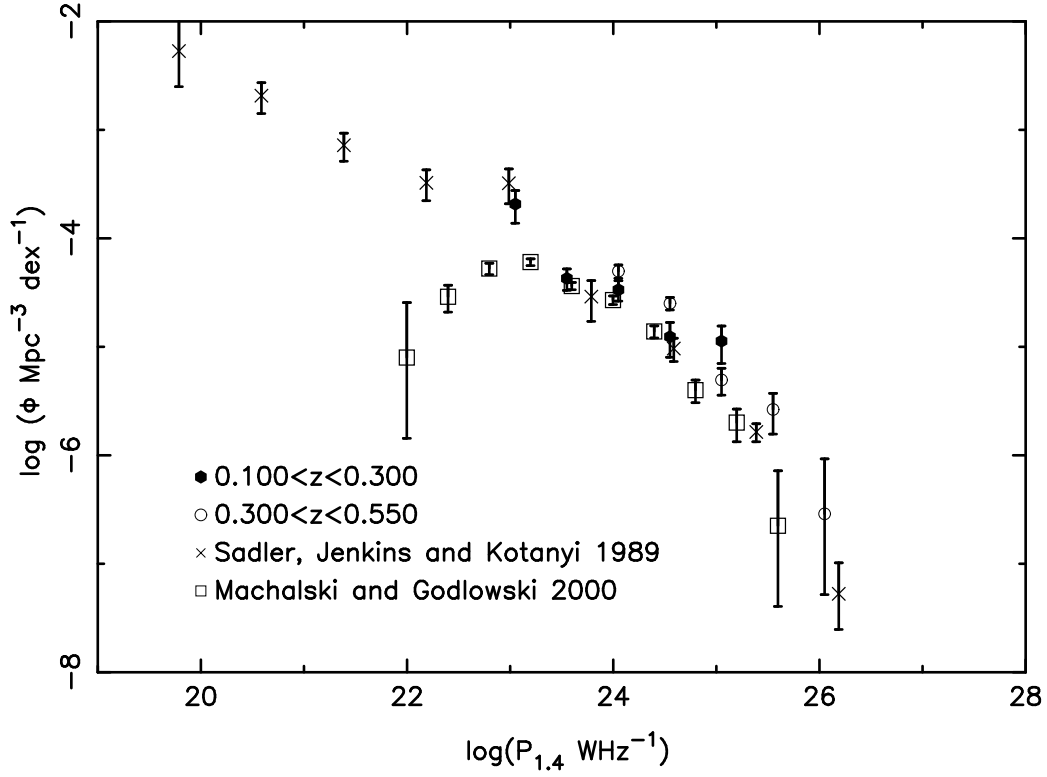
Fig. 7.— The luminosity function of radio galaxies detected in the Panoramic Deep Fields. Estimates of the luminosity function have been corrected for incompleteness. For several luminosity bins, the estimate of the space density of $0.30 < z < 0.55$ radio galaxies is significantly higher than the estimates for $0.10 < z < 0.30$ radio galaxies.
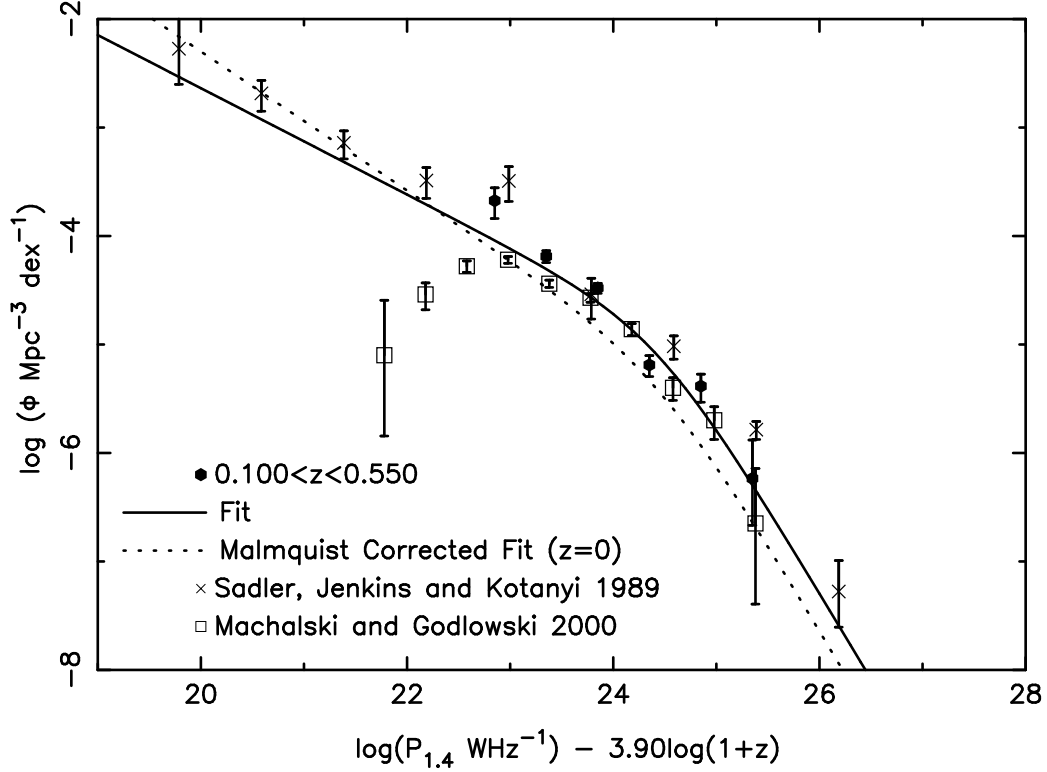
Fig. 8.— The luminosity function of radio galaxies at the current epoch where the luminosity at $z \sim 0$ has been estimated by dividing the radio power by $(1 + z)^{3.9}$. The Machalski and Godlowski (2000) data points have been shifted assuming $z = 0.15$. There is reasonable agreement between the model of the luminosity function, the data and low redshift surveys with the exception of $P < 10^{23} \mathrm{WHz}^{-1}$ radio galaxies from Machalski and Godlowski (2000). As the size of the Panoramic Deep Fields sample is comparable to low redshift samples, the Poisson errors of the luminosity function estimates are comparable to Sadler et al. (1989) and Machalski and Godlowski (2000).

Table 1.   Several previous samples of radio galaxies (excluding QSOs)

Survey	Frequency (GHz)	Flux Limit (mJy)	Mag. Limit	Spectroscopic Redshifts	Photometric Redshifts
Kuehr et al. (1981)	5.0	1000	$V \sim 23$	118	-
Peacock and Wall (1981)	2.7	1500	$V \sim 22$	62	-
Wall and Peacock (1985)	2.7	2000	$V \sim 24$	107	37
Wall and Peacock (1985) $z > 0.3$	2.7	2000	$V \sim 24$	14	27
Condon (1989)	1.4	0.5	$B_T = 12.0$	92	-
Dunlop et al. (1989)	2.7	100	$R \sim 24$	36	78
Dunlop et al. (1989) $z > 0.3$	2.7	100	$R \sim 24$	14	73
Sadler et al. (1989)	5.0	0.8	$B_T = 13.8$	49	-
Rowan-Robinson et al. (1993)	1.4	0.1	$B \sim 22$	8	3
Hopkins et al. (1998)	1.4	0.2	$R < 21.5$	63	-
Sadler et al. (1999)	1.4	2.5	$B_J = 19.4$	52	-
Machalski and Condon (1999)	1.4	2.5	$R \sim 18.5$	387	162
Panoramic Deep Fields $z > 0.1$	1.4	5.0	$B_J = 23.5$	-	230
Panoramic Deep Fields $z > 0.3$	1.4	5.0	$B_J = 23.5$	-	164
Panoramic Deep Fields $z > 0.5$	1.4	5.0	$B_J = 23.5$	-	58

Table 2.   Radio Galaxy Catalogue

NVSS Source	RA (J2000)	Declination (J2000)	$S_{1.4}$ (mJy)	B_J	$U - B_J$	$B_J - R$	$R - I$	Photo z	Optical-NVSS Offset
J004407-294751	00 44 07.8	-29 47 49.7	95.7	23.24	-	2.35	-	0.581	1.7″
J004432-285650	00 44 32.9	-28 56 48.3	8.3	22.38	-	2.30	1.33	0.531	2.2″
J004434-295222	00 44 34.0	-29 52 24.0	7.8	23.17	-	2.94	0.51	0.618	1.4″
J004443-300606	00 44 43.6	-30 06 04.6	5.6	22.00	-	2.32	1.10	0.482	1.6″
J004514-292851	00 45 14.5	-29 28 51.2	16.0	22.10	-	2.59	0.76	0.501	1.7″
J004607-282301	00 46 07.7	-28 22 58.8	5.7	21.70	-	2.11	0.79	0.421	2.9″
J004633-290137	00 46 34.0	-29 01 40.1	7.2	18.76	0.96	1.80	0.61	0.198	3.1″
J004637-295324	00 46 37.7	-29 53 31.1	37.2	20.54	0.65	1.63	0.71	0.285	7.4″
J004649-300729	00 46 49.6	-30 07 28.9	29.2	22.79	-	2.03	-	0.488	2.1″
J004658-273304	00 46 58.6	-27 33 03.5	15.0	20.04	-	2.11	0.63	0.297	1.3″
J004702-271740	00 47 02.8	-27 17 42.2	7.7	21.88	-	2.66	0.87	0.496	2.5″
J004723-273111	00 47 23.0	-27 31 10.8	17.4	22.04	-	2.63	1.18	0.525	0.7″
J004725-292157	00 47 24.9	-29 22 00.3	8.1	22.87	-	2.80	1.25	0.629	4.7″
J004741-270435	00 47 41.8	-27 04 34.8	7.3	19.85	-	2.28	0.72	0.304	2.0″
J004752-284403	00 47 52.1	-28 44 04.2	39.8	23.13	-	2.10	-	0.544	1.1″
J004808-281054	00 48 08.5	-28 10 51.8	14.3	22.62	-	2.72	1.53	0.618	4.0″
J004827-290607	00 48 27.4	-29 06 03.0	15.5	18.95	0.96	1.83	0.77	0.209	5.1″
J004831-294207	00 48 31.5	-29 42 09.1	7.7	22.42	-	2.02	1.84	0.542	3.0″
J004836-272938	00 48 36.1	-27 29 42.8	6.9	20.58	1.33	2.16	1.17	0.355	4.9″
J004925-300237	00 49 25.6	-30 02 37.5	8.4	19.72	0.32	1.45	1.00	0.221	0.3″
J004954-282535	00 49 54.9	-28 25 35.8	8.9	21.07	-	2.45	0.88	0.409	1.4″
J005049-280409	00 50 49.3	-28 04 09.4	33.8	21.89	-	2.30	0.29	0.436	0.8″
J005106-262606	00 51 06.6	-26 26 01.0	5.0	22.27	-	2.14	0.53	0.461	5.3″
J005109-300851	00 51 09.6	-30 08 52.1	10.3	20.90	-	2.30	0.91	0.382	1.4″
J005116-283144	00 51 15.6	-28 31 32.2	53.8	17.49	0.75	1.51	0.76	0.102	14.4″
J005116-272049	00 51 16.4	-27 20 46.7	12.9	21.31	-	2.22	0.75	0.398	3.2″
J005127-282926	00 51 27.5	-28 29 23.4	77.8	18.38	0.46	1.36	1.17	0.128	3.0″
J005127-282926	00 51 28.1	-28 29 26.9	77.8	17.70	0.61	1.44	1.05	0.104	10.7″
J005132-282442	00 51 32.6	-28 24 51.7	92.1	17.54	0.72	1.53	0.82	0.102	8.9″
J005209-263054	00 52 09.6	-26 30 55.5	10.1	22.16	-	2.14	0.43	0.448	1.9″
J005216-253041	00 52 16.2	-25 30 43.2	11.0	21.75	-	2.66	0.70	0.475	2.8″
J005223-284112	00 52 23.9	-28 41 10.2	7.8	23.50	-	2.50	1.41	0.674	3.5″
J005302-254755	00 53 02.4	-25 47 56.5	22.0	22.21	-	2.68	1.10	0.540	4.2″
J005304-281612	00 53 04.9	-28 16 13.9	9.9	23.12	-	2.04	-	0.590	2.8″
J005312-293605	00 53 12.7	-29 36 09.1	22.9	22.85	-	2.01	-	0.490	3.9″
J005321-291448	00 53 21.2	-29 14 49.3	47.5	21.09	0.03	1.87	1.06	0.358	0.9″
J005347-290652	00 53 47.6	-29 06 49.7	6.4	22.23	-	2.54	1.19	0.533	4.8″
J005400-265729	00 54 01.0	-26 57 27.9	16.6	21.52	-0.18	2.22	0.92	0.423	1.9″
J005400-282116	00 54 01.1	-28 21 15.8	9.5	20.79	-	2.28	1.05	0.377	2.7″
J005422-292720	00 54 22.3	-29 27 27.4	19.9	19.40	0.63	1.79	0.53	0.229	7.9″
J005422-294000	00 54 22.5	-29 40 02.9	18.0	22.14	-	2.02	1.57	0.493	2.6″
J005438-253357	00 54 37.8	-25 33 56.4	5.3	21.81	-	2.38	1.09	0.472	3.3″
J005440-253946	00 54 40.7	-25 39 43.6	7.0	18.32	0.47	1.42	0.84	0.132	3.8″
J005512-270947	00 55 12.5	-27 09 47.0	11.3	19.96	0.63	1.60	0.71	0.244	0.1″
J005513-275208	00 55 13.3	-27 52 07.7	19.1	22.76	-	2.34	1.66	0.598	4.1″
J005515-253900	00 55 15.7	-25 38 59.8	7.8	20.70	-	2.06	0.85	0.341	1.3″
J005530-272329	00 55 31.0	-27 23 30.2	6.5	21.96	-	2.52	0.84	0.486	1.2″
J005542-275056	00 55 42.2	-27 50 55.9	6.2	23.16	-1.51	2.39	-	0.689	4.6″

Table 2—Continued

NVSS Source	RA (J2000)	Declination (J2000)	$S_{1.4}$ (mJy)	B_J	$U - B_J$	$B_J - R$	$R - I$	Photo z	Optical-NVSS Offset
J005548-283609	00 55 48.7	-28 36 06.4	10.4	22.87	-	2.43	2.20	0.674	3.6″
J005608-262507	00 56 08.1	-26 25 06.0	163.7	21.87	-	2.56	0.02	0.450	1.5″
J005609-283406	00 56 09.3	-28 34 02.4	48.4	18.16	0.77	1.65	0.94	0.125	4.7″
J005613-285535	00 56 13.7	-28 55 35.2	8.0	18.03	0.86	1.62	0.96	0.122	1.4″
J005630-272949	00 56 30.1	-27 29 49.9	86.1	19.61	0.78	1.68	0.78	0.231	0.3″
J005642-254144	00 56 42.3	-25 41 44.0	68.7	23.38	-	3.08	1.75	0.763	0.4″
J005642-264710	00 56 42.4	-26 47 07.8	22.9	20.14	-	2.38	0.88	0.336	3.8″
J005647-254337	00 56 48.0	-25 43 37.7	8.6	22.58	-	2.39	0.89	0.531	2.6″
J005651-295815	00 56 50.9	-29 58 13.8	9.3	18.85	0.62	1.56	0.73	0.172	2.8″
J005656-254626	00 56 56.4	-25 46 28.8	16.2	21.91	-	2.29	1.12	0.473	3.0″
J005700-260929	00 57 00.9	-26 09 29.0	5.3	22.50	-	2.35	1.01	0.526	0.3″
J005708-254408	00 57 08.8	-25 44 10.1	12.2	21.89	-	2.83	0.42	0.491	2.1″
J005722-290716	00 57 22.9	-29 07 18.3	6.8	21.45	-	2.28	0.85	0.420	4.5″
J005725-264830	00 57 25.5	-26 48 37.8	9.5	19.65	0.74	1.48	0.61	0.217	7.6″
J005725-264830	00 57 25.7	-26 48 25.6	9.5	18.50	0.62	1.55	0.77	0.152	6.0″
J005733-295315	00 57 33.4	-29 53 11.4	5.4	22.53	-	2.41	1.54	0.572	5.2″
J005742-253316	00 57 42.8	-25 33 16.1	238.4	21.61	-	1.99	1.11	0.414	1.5″
J005756-252236	00 57 57.0	-25 22 37.3	301.9	18.99	0.87	1.71	0.77	0.200	1.2″
J005820-251830	00 58 21.0	-25 18 26.6	19.1	19.93	1.58	2.03	0.90	0.287	3.6″
J005823-290428	00 58 23.3	-29 04 28.5	17.7	18.99	0.89	1.86	0.70	0.215	0.4″
J005829-285905	00 58 29.2	-28 59 06.6	30.3	18.85	0.18	1.66	0.90	0.188	1.7″
J005832-292614	00 58 32.7	-29 26 15.6	56.2	22.29	-	2.18	1.11	0.495	1.4″
J005833-263224	00 58 33.2	-26 32 25.7	25.1	22.99	-	2.42	0.93	0.575	1.5″
J005848-280106	00 58 48.5	-28 01 07.4	19.2	19.77	0.97	1.94	0.69	0.264	2.8″
J005854-292657	00 58 54.9	-29 26 58.4	17.0	21.11	0.08	2.06	1.15	0.383	2.1″
J005908-285949	00 59 09.2	-28 59 44.2	448.2	17.92	0.97	1.80	0.74	0.120	8.4″
J005916-253847	00 59 16.4	-25 38 49.3	6.6	20.24	-	2.29	0.68	0.328	1.6″
J005936-252155	00 59 36.9	-25 21 54.2	8.4	21.19	-	2.29	0.87	0.401	1.5″
J005945-300925	00 59 45.7	-30 09 24.9	8.9	21.60	-	2.59	1.11	0.479	3.7″
J005953-281831	00 59 53.3	-28 18 28.2	5.1	20.39	-	1.98	1.27	0.326	4.3″
J010001-291945	01 00 01.1	-29 19 46.0	19.0	19.68	0.97	1.81	0.57	0.246	2.2″
J010004-261114	01 00 04.2	-26 11 17.3	12.6	21.30	-	2.01	1.00	0.386	3.1″
J010004-261114	01 00 04.5	-26 11 11.5	12.6	22.90	-	2.28	-	0.516	5.5″
J010006-283206	01 00 07.0	-28 32 09.3	16.9	20.58	-	2.21	1.11	0.357	4.6″
J010010-260651	01 00 10.9	-26 06 55.0	5.3	22.65	-	2.39	1.44	0.576	4.1″
J010030-263353	01 00 31.0	-26 33 53.0	98.8	22.10	-	2.32	1.89	0.549	1.4″
J010048-274021	01 00 49.0	-27 40 23.3	20.0	20.37	1.53	2.23	1.00	0.340	1.9″
J010102-285840	01 01 02.4	-28 58 46.9	18.7	19.80	1.10	2.13	0.83	0.288	6.8″
J010114-284021	01 01 14.1	-28 40 17.9	18.9	20.60	-	2.26	0.54	0.345	4.3″
J010129-272202	01 01 29.9	-27 22 01.9	8.6	19.66	1.22	1.95	0.83	0.262	0.5″
J010132-275444	01 01 32.3	-27 54 44.1	18.4	22.83	-2.18	2.65	1.00	0.588	0.8″
J010139-291502	01 01 39.6	-29 15 02.1	17.8	22.41	-	2.45	-	0.512	1.9″
J010144-261730	01 01 44.5	-26 17 29.0	11.4	22.48	-	2.68	1.27	0.578	5.3″
J010204-294201	01 02 04.1	-29 42 03.5	26.9	21.89	-	2.30	0.60	0.446	5.1″
J010212-253733	01 02 13.0	-25 37 31.3	6.3	20.85	-	2.17	0.56	0.354	3.9″
J010312-251758	01 03 12.5	-25 18 01.4	16.6	21.52	-	2.20	0.98	0.423	3.1″
J010312-251758	01 03 12.7	-25 17 55.1	16.6	21.88	-	2.60	0.28	0.462	4.2″
J010320-254037	01 03 19.8	-25 40 35.3	8.2	20.16	1.38	1.91	0.53	0.283	4.4″

Table 2—Continued

NVSS Source	RA (J2000)	Declination (J2000)	$S_{1.4}$ (mJy)	B_J	$U - B_J$	$B_J - R$	$R - I$	Photo z	Optical-NVSS Offset
J010325-282000	01 03 25.9	-28 20 00.3	12.4	19.55	1.18	1.80	0.64	0.238	1.0″
J010401-300109	01 04 01.5	-30 01 06.1	6.1	20.92	-	2.58	0.54	0.399	3.7″
J010407-293616	01 04 07.5	-29 36 21.1	5.8	18.00	0.82	1.51	0.88	0.124	5.9″
J010422-254751	01 04 22.1	-25 47 51.1	61.2	22.84	-	2.17	1.55	0.578	4.6″
J010438-300451	01 04 37.9	-30 04 51.9	12.0	20.78	-	2.16	0.84	0.356	3.4″
J010448-261248	01 04 48.5	-26 12 50.0	8.2	22.45	-	2.54	-	0.530	3.1″
J010449-283020	01 04 49.8	-28 30 24.4	8.9	21.84	-	2.81	1.01	0.517	4.7″
J010451-251721	01 04 51.6	-25 17 24.8	10.0	20.57	1.32	1.94	0.98	0.324	5.6″
J010453-262220	01 04 53.4	-26 22 21.0	18.7	21.55	-	2.25	0.65	0.416	1.1″
J010456-294043	01 04 56.9	-29 40 43.2	30.2	19.94	1.57	2.08	0.77	0.290	1.2″
J010520-252313	01 05 21.0	-25 23 10.5	8.3	18.76	1.13	1.73	0.75	0.191	3.0″
J010525-263141	01 05 25.1	-26 31 44.9	5.0	20.95	-	1.78	0.94	0.334	4.1″
J010527-281043	01 05 28.2	-28 10 42.9	10.9	19.13	1.03	1.58	0.69	0.195	4.6″
J010542-295441	01 05 42.5	-29 54 42.7	7.0	20.90	-	2.11	0.49	0.350	1.9″
J010545-254751	01 05 45.3	-25 47 52.6	34.5	19.96	-	2.25	0.68	0.306	1.1″
J010545-295033	01 05 45.7	-29 50 32.5	12.3	21.19	-	2.19	0.70	0.385	0.7″
J010547-285728	01 05 47.8	-28 57 28.2	18.2	19.25	0.65	1.73	0.86	0.217	1.0″
J010607-280935	01 06 07.2	-28 09 34.4	10.9	22.92	-1.29	2.07	-	0.500	1.0″
J010610-262431	01 06 10.7	-26 24 31.0	63.9	20.34	-	2.21	0.95	0.335	1.1″
J010625-284913	01 06 25.9	-28 49 16.7	12.1	21.73	-	2.63	0.68	0.470	3.9″
J010632-261545	01 06 32.4	-26 15 42.6	11.6	21.64	-	1.86	0.82	0.392	4.0″
J010633-285055	01 06 33.5	-28 50 53.6	12.0	20.52	0.84	2.00	0.84	0.322	3.0″
J103241+013424	10 32 41.0	+01 34 24.7	9.2	22.86	-	2.29	1.80	0.598	0.6″
J103409+021227	10 34 09.1	+02 12 26.0	9.2	20.35	0.13	2.00	0.79	0.301	2.5″
J103414+000521	10 34 14.6	+00 05 21.4	254.8	19.43	0.57	1.49	0.73	0.181	4.6″
J103418-002030	10 34 19.1	-00 20 32.1	5.0	18.53	0.44	1.34	0.70	0.122	2.9″
J103424-021102	10 34 24.4	-02 11 02.6	123.5	20.41	0.69	1.75	0.58	0.270	0.5″
J103431+012356	10 34 31.2	+01 23 55.7	15.9	22.52	-	2.28	1.36	0.526	0.4″
J103453+003637	10 34 54.0	+00 36 37.8	139.1	22.34	-	2.26	0.94	0.471	0.5″
J103456-001007	10 34 56.9	-00 10 04.3	6.3	21.65	-	2.13	0.75	0.389	3.8″
J103514-002432	10 35 15.0	-00 24 30.8	16.9	21.76	-	2.53	0.78	0.437	1.5″
J103516+003242	10 35 16.2	+00 32 41.2	17.1	22.62	-	2.67	1.48	0.577	1.2″
J103521+012020	10 35 20.9	+01 20 23.3	5.5	22.82	-	2.07	1.24	0.526	4.0″
J103525-000145	10 35 25.4	-00 01 40.8	7.8	21.79	-	2.38	0.81	0.426	4.5″
J103526-012513	10 35 26.3	-01 25 13.1	7.3	21.46	-	2.18	0.90	0.388	1.3″
J103552-004246	10 35 52.0	-00 42 45.6	6.1	22.13	-	2.76	1.02	0.508	0.9″
J103609+013721	10 36 09.0	+01 37 20.7	11.0	21.51	-	2.30	0.78	0.412	1.2″
J103614-022237	10 36 14.8	-02 22 36.2	28.1	20.41	-	1.91	0.85	0.289	2.2″
J103618+011403	10 36 19.2	+01 14 07.6	13.4	20.38	-	2.37	-0.08	0.324	5.7″
J103619-001955	10 36 19.8	-00 19 55.8	8.4	20.64	1.17	2.03	0.81	0.306	0.7″
J103623+011118	10 36 23.0	+01 11 19.7	5.8	21.96	-	2.52	1.21	0.492	1.9″
J103647-004055	10 36 47.2	-00 40 56.2	12.9	19.07	0.77	1.58	0.83	0.168	2.4″
J103700+014542	10 37 00.5	+01 45 39.5	44.7	22.34	-	2.69	0.92	0.531	3.8″
J103705-015607	10 37 05.8	-01 56 06.1	45.5	22.02	-	2.93	-0.34	0.465	1.2″
J103737-004111	10 37 36.9	-00 41 17.5	29.4	18.17	0.71	1.70	0.74	0.118	7.8″
J103740-012801	10 37 40.9	-01 27 59.8	81.8	21.77	-	2.25	0.84	0.420	3.6″
J103749-000521	10 37 49.2	-00 05 22.9	32.0	21.54	-	1.89	1.18	0.373	2.3″
J103828-002932	10 38 29.0	-00 29 34.1	5.3	20.90	-	2.53	0.84	0.384	4.5″

Table 2—Continued

NVSS Source	RA (J2000)	Declination (J2000)	$S_{1.4}$ (mJy)	B_J	$U - B_J$	$B_J - R$	$R - I$	Photo z	Optical-NVSS Offset
J103834+011924	10 38 34.9	+01 19 23.2	6.8	20.77	1.42	2.08	0.92	0.339	2.3″
J103836+011753	10 38 36.8	+01 18 00.7	321.4	19.72	0.75	1.62	0.91	0.217	6.8″
J103843-020738	10 38 43.4	-02 07 36.2	6.6	21.61	-	2.44	0.93	0.431	4.0″
J103850-013928	10 38 50.0	-01 39 25.4	10.9	20.91	0.36	1.72	0.31	0.296	4.2″
J103855-015040	10 38 55.6	-01 50 43.2	9.9	21.11	-	2.28	0.80	0.371	3.6″
J103908-023917	10 39 08.8	-02 39 22.8	26.5	20.77	0.03	1.76	0.35	0.293	5.5″
J103911+013800	10 39 11.2	+01 38 01.2	24.0	21.36	-	2.09	0.71	0.381	1.4″
J103920+010510	10 39 20.4	+01 05 14.5	8.3	18.61	0.67	1.85	0.94	0.185	6.1″
J103938+003046	10 39 38.4	+00 30 46.4	8.4	18.20	0.63	1.55	0.90	0.117	1.4″
J103943+011955	10 39 43.3	+01 19 55.3	126.5	21.37	-	2.76	-0.43	0.414	4.1″
J103944-021125	10 39 44.2	-02 11 28.0	29.7	22.87	-	2.80	1.25	0.601	3.0″
J103956-024041	10 39 57.0	-02 40 43.2	5.3	22.38	-	2.25	0.72	0.466	1.7″
J104006+012304	10 40 05.8	+01 23 03.4	5.3	21.85	-	2.30	1.24	0.462	2.8″
J104014-023503	10 40 14.9	-02 35 04.0	17.3	22.33	-	2.55	1.05	0.509	0.8″
J104020+010507	10 40 20.3	+01 05 05.4	11.2	22.46	-	2.02	-	0.441	3.1″
J104037+004223	10 40 37.8	+00 42 21.9	15.9	21.80	-	2.59	0.99	0.463	1.3″
J104039+013658	10 40 39.7	+01 37 03.9	5.6	19.78	1.39	2.02	1.07	0.272	5.6″
J104044+020535	10 40 44.9	+02 05 33.4	20.0	21.84	-	2.46	0.71	0.453	2.4″
J104105-004334	10 41 05.2	-00 43 37.4	27.0	19.00	0.63	1.41	1.12	0.151	3.0″
J104106+011904	10 41 06.3	+01 19 03.8	11.0	22.15	-	2.55	1.23	0.514	0.5″
J104118+001052	10 41 18.1	+00 10 47.6	6.3	21.74	-	2.45	0.84	0.439	4.9″
J104121-022303	10 41 21.5	-02 23 01.1	7.9	19.18	0.70	1.97	0.70	0.217	2.8″
J104122+020900	10 41 22.9	+02 09 02.2	250.4	21.66	-	2.18	1.34	0.439	2.2″
J104129-003759	10 41 29.1	-00 38 00.3	47.5	17.86	0.64	1.72	0.85	0.104	0.5″
J104131-002736	10 41 31.9	-00 27 33.4	13.7	17.86	0.76	1.73	0.94	0.105	4.4″
J104138-005412	10 41 39.0	-00 54 16.3	20.6	22.65	-	3.05	1.32	0.619	4.2″
J104159-020144	10 41 59.6	-02 01 43.9	48.6	20.07	1.69	2.30	0.91	0.305	3.1″
J104208-002116	10 42 08.4	-00 21 15.4	28.9	21.08	-0.35	1.73	0.86	0.322	1.1″
J104212+015213	10 42 12.5	+01 52 12.1	28.5	19.74	0.82	2.07	0.84	0.268	1.7″
J104216+012004	10 42 16.2	+01 20 02.7	23.5	21.79	-	1.96	1.50	0.435	1.4″
J104231+003902	10 42 31.5	+00 39 06.7	9.8	21.64	-	2.40	0.60	0.417	4.7″
J104241-000947	10 42 41.7	-00 09 45.9	12.5	22.38	-	2.02	1.06	0.465	1.6″
J104246-022758	10 42 46.9	-02 27 57.2	7.8	22.85	-	2.20	1.59	0.552	1.7″
J104250+003355	10 42 51.0	+00 33 54.2	5.8	21.70	-	2.19	0.74	0.407	3.2″
J104301+010648	10 43 01.6	+01 06 54.6	10.9	19.72	1.08	2.03	0.91	0.263	6.5″
J104302+005051	10 43 02.3	+00 50 47.5	56.9	19.90	1.55	2.09	0.81	0.275	7.5″
J104336+011624	10 43 35.8	+01 16 28.5	99.2	19.79	0.48	1.78	0.61	0.239	5.1″
J104335-000736	10 43 35.8	-00 07 34.0	20.8	21.22	-	2.41	0.71	0.395	4.7″
J104339-000008	10 43 39.8	-00 00 14.0	5.7	19.37	0.26	1.48	0.88	0.187	5.9″
J104346+010038	10 43 46.0	+01 00 41.8	13.0	23.26	-	2.45	1.36	0.618	3.5″
J104347-012404	10 43 48.0	-01 24 00.2	8.7	20.96	-	2.23	0.79	0.358	4.2″
J104352+000600	10 43 52.4	+00 06 03.7	7.5	22.39	-	2.88	0.99	0.550	3.4″
J104412-023829	10 44 12.6	-02 38 31.1	5.8	20.01	-	2.06	0.51	0.272	1.3″
J104414-015147	10 44 14.3	-01 51 47.7	6.8	19.87	0.99	1.84	0.75	0.247	5.8″
J104415-010945	10 44 15.8	-01 09 46.7	15.6	21.47	-0.47	1.97	-	0.393	1.8″
J104416+020004	10 44 16.1	+02 00 05.4	26.2	23.07	-	2.02	-	0.494	2.2″
J104420-011146	10 44 20.3	-01 11 50.2	276.0	22.67	-	2.05	-	0.462	3.7″
J104455+005654	10 44 55.0	+00 56 55.3	16.6	18.06	0.56	1.58	0.86	0.113	2.6″

Table 2—Continued

NVSS Source	RA (J2000)	Declination (J2000)	$S_{1.4}$ (mJy)	B_J	$U - B_J$	$B_J - R$	$R - I$	Photo z	Optical-NVSS Offset
J104509-015843	10 45 09.4	-01 58 43.0	9.7	22.29	-	2.58	1.03	0.512	1.4″
J104513-004931	10 45 13.4	-00 49 29.9	7.4	21.46	-	2.63	0.76	0.438	3.0″
J104513+014557	10 45 13.8	+01 45 57.1	10.1	21.28	-	2.71	0.91	0.438	2.8″
J104516-010605	10 45 16.5	-01 06 07.2	12.5	20.70	-	1.98	0.88	0.320	2.1″
J104524+001240	10 45 25.0	+00 12 41.1	10.6	22.53	-	2.35	0.62	0.492	0.6″
J104537+000119	10 45 37.3	+00 01 16.3	14.7	20.69	-	2.34	0.92	0.357	3.3″
J104555+002811	10 45 54.8	+00 28 10.6	9.1	21.35	0.43	2.29	0.90	0.401	3.5″
J104603+014906	10 46 03.8	+01 49 07.0	18.3	21.67	-	2.55	0.84	0.449	1.9″
J104603-023014	10 46 03.8	-02 30 14.4	10.6	22.66	-	2.95	0.75	0.571	0.7″
J104630-001215	10 46 30.6	-00 12 12.9	6.5	21.50	-	2.24	0.86	0.407	3.5″
J104632-011340	10 46 32.4	-01 13 37.9	133.7	19.40	0.83	1.59	0.65	0.201	2.5″
J104633-021714	10 46 33.1	-02 17 12.8	38.1	18.67	0.83	1.72	0.74	0.176	2.4″
J104650-000114	10 46 50.8	-00 01 09.9	35.6	22.41	-	2.09	0.60	0.458	5.5″
J104650-000114	10 46 50.9	-00 01 15.4	35.6	21.05	-	2.49	0.94	0.403	0.9″
J104658-014729	10 46 58.4	-01 47 25.7	11.5	22.73	-	2.69	1.85	0.634	3.8″
J104723-021851	10 47 23.7	-02 18 49.3	30.3	20.65	-	1.98	0.69	0.314	4.0″
J104733+001526	10 47 33.5	+00 15 26.2	49.7	23.40	-	2.49	1.50	0.652	1.0″
J104738-022255	10 47 38.7	-02 22 58.9	214.4	19.97	0.32	1.77	0.66	0.249	3.7″
J104744+013632	10 47 44.2	+01 36 37.5	28.9	23.65	-	2.20	-	0.572	4.7″
J104754+012906	10 47 54.8	+01 29 00.1	9.6	19.07	1.01	2.03	0.83	0.226	6.5″
J104801-013016	10 48 01.9	-01 30 14.8	5.4	18.04	0.26	1.42	0.81	0.104	3.2″
J104805+000858	10 48 05.8	+00 08 58.7	47.8	22.84	-	2.82	0.97	0.592	0.7″
J104828+003949	10 48 28.7	+00 39 38.4	5.2	18.24	0.35	1.37	0.91	0.116	12.0″
J104849-011226	10 48 50.0	-01 12 26.8	5.9	21.23	-	2.33	0.89	0.398	1.9″
J104905-015747	10 49 05.3	-01 57 47.1	9.0	22.00	-	1.98	0.88	0.424	2.0″
J104910-003637	10 49 10.6	-00 36 40.2	18.2	23.32	-	2.88	1.62	0.699	3.5″
J104923+000027	10 49 23.1	+00 00 27.6	23.2	22.32	-	2.74	0.72	0.519	0.7″
J104926-000343	10 49 26.4	-00 03 47.9	6.7	20.48	-	2.24	0.79	0.330	4.4″
J104926+005608	10 49 26.5	+00 56 09.2	33.9	18.46	0.49	1.66	0.75	0.147	1.1″
J104928-022728	10 49 28.6	-02 27 29.4	8.2	18.88	0.91	1.77	0.73	0.193	1.8″
J104933-002743	10 49 33.9	-00 27 40.9	15.3	23.58	-	2.26	0.97	0.605	2.6″
J104958-022621	10 49 58.4	-02 26 23.7	14.7	22.81	-	2.60	0.99	0.566	1.9″
J105026-020427	10 50 26.9	-02 04 25.6	14.4	21.82	-	1.98	1.30	0.430	3.6″
J105036-023618	10 50 36.5	-02 36 15.9	14.5	17.86	0.70	1.58	0.92	0.108	2.5″
J105037-004722	10 50 37.4	-00 47 24.4	125.7	23.14	-	2.30	-	0.594	3.9″
J105045+004540	10 50 45.5	+00 45 42.0	6.4	20.01	1.08	1.94	0.74	0.267	4.7″
J105047+010738	10 50 47.4	+01 07 39.5	30.4	23.44	-	2.32	1.44	0.628	1.0″
J105101-001739	10 51 01.2	-00 17 39.0	16.5	20.49	-	2.08	0.92	0.317	1.9″
J105103-021302	10 51 03.7	-02 12 59.4	6.6	22.86	-	2.01	0.71	0.498	3.3″
J105111-021317	10 51 11.1	-02 13 16.5	31.6	19.42	0.30	1.67	0.75	0.211	1.1″
J105112-011509	10 51 12.3	-01 15 10.1	23.7	20.67	-	2.32	0.80	0.348	1.1″
J105120-014300	10 51 20.6	-01 42 58.2	6.3	20.24	1.83	2.10	0.76	0.301	3.2″
J105126-014404	10 51 26.2	-01 44 02.7	17.2	22.84	-	2.79	0.82	0.580	2.8″
J105138-011919	10 51 38.5	-01 19 20.7	5.2	18.12	0.85	1.58	0.70	0.126	1.5″
J105140-022845	10 51 40.6	-02 28 46.6	5.9	19.83	2.23	2.10	0.71	0.274	5.6″
J105150+011351	10 51 50.7	+01 13 51.4	10.1	23.39	-	2.45	0.67	0.583	2.2″
J105151+010312	10 51 51.7	+01 03 16.4	16.3	21.19	0.68	2.67	0.76	0.420	3.9″
J105158+005045	10 51 58.9	+00 50 45.3	13.8	20.90	-	2.68	0.69	0.398	0.9″

Table 2—Continued

NVSS Source	RA (J2000)	Declination (J2000)	$S_{1.4}$ (mJy)	B_J	$U - B_J$	$B_J - R$	$R - I$	Photo z	Optical-NVSS Offset
J105158+005045	10 51 59.5	+00 50 47.6	13.8	18.84	0.89	1.66	1.29	0.155	9.2″
J105227-014110	10 52 27.1	-01 41 08.0	23.3	21.89	-	2.29	0.54	0.432	3.7″

Table 3. The Radio Galaxy Luminosity Function. Where $k_L = 3.9$, the radio powers have been divided by the luminosity evolution to estimate the luminosity function at $z \sim 0$.

Redshift Range	k_L	$\mathrm{Log}(P_{1.4}\mathrm{WHz}^{-1})$	N_{gal}	$\Phi\ (h^3\mathrm{Mpc}^{-3}\mathrm{dex}^{-1})$
$0.10 < z < 0.30$	0.0	23.05	9	$2.1 \pm^{0.9}_{0.7} \times 10^{-4}$
$0.10 < z < 0.30$	0.0	23.55	20	$4.2 \pm 1.0 \times 10^{-5}$
$0.10 < z < 0.30$	0.0	24.05	22	$3.3 \pm 0.7 \times 10^{-5}$
$0.10 < z < 0.30$	0.0	24.55	8	$1.2 \pm^{0.6}_{0.4} \times 10^{-5}$
$0.10 < z < 0.30$	0.0	25.05	7	$1.1 \pm^{0.6}_{0.4} \times 10^{-6}$
$0.30 < z < 0.55$	0.0	24.05	51	$5.0 \pm 0.7 \times 10^{-5}$
$0.30 < z < 0.55$	0.0	24.55	57	$2.5 \pm 0.3 \times 10^{-5}$
$0.30 < z < 0.55$	0.0	25.05	13	$5.0 \pm^{1.8}_{1.0} \times 10^{-6}$
$0.30 < z < 0.55$	0.0	25.55	6	$2.7 \pm^{1.5}_{1.0} \times 10^{-6}$
$0.30 < z < 0.55$	0.0	26.05	1	$0.3 \pm^{0.6}_{0.2} \times 10^{-6}$
$0.10 < z < 0.55$	3.9	22.85	10	$2.1 \pm^{0.9}_{0.6} \times 10^{-4}$
$0.10 < z < 0.55$	3.9	23.35	63	$6.5 \pm 0.8 \times 10^{-5}$
$0.10 < z < 0.55$	3.9	23.85	87	$3.3 \pm 0.4 \times 10^{-5}$
$0.10 < z < 0.55$	3.9	24.35	21	$6.5 \pm 1.4 \times 10^{-6}$
$0.10 < z < 0.55$	3.9	24.85	12	$4.1 \pm^{1.5}_{0.9} \times 10^{-6}$
$0.10 < z < 0.55$	3.9	25.35	2	$5.8 \pm^{7.4}_{3.7} \times 10^{-7}$

Table 4. The Radio Galaxy Luminosity Function Parameters

Parameter	Best-Fit Estimate	Malmquist Corrected	$\alpha_r = 0.5$ Estimate
$C^*_{1.4}[h^3\mathrm{Mpc}^{-3}]$	$(1.5 \pm 0.4) \times 10^{-5}$	$(0.7 \pm 0.2) \times 10^{-5}$	$(1.5 \pm 0.4) \times 10^{-5}$
$P^*_{1.4}[\mathrm{WHz}^{-1}]$	$(2.8 \pm 0.9) \times 10^{24}$	$(3.2 \pm 1.0) \times 10^{24}$	$(3.7 \pm 1.2) \times 10^{24}$
α	-1.59 ± 0.10	-1.61 ± 0.10	-1.71 ± 0.07
β	-0.49 ± 0.08	-0.64 ± 0.11	-0.44 ± 0.07
k_L	3.9 ± 1.1	4.9 ± 1.4	3.3 ± 1.1
P_{KS}	0.14	-	0.20